applied optics

Identifying sampling comb changes in Fourier transform spectrometers with significant self-emission and beam splitter absorption

J. Brasunas,[1,*] A. Mamoutkine,[2] and N. Gorius[3]

[1]NASA Goddard Space Flight Center, Code 693, Greenbelt, Maryland 20771, USA
[2]Adnet Systems, 8800 Greenbelt Road, Code 693, Greenbelt, Maryland 20771, USA
[3]Catholic University, 8800 Greenbelt Road, Code 693, Greenbelt, Maryland 20771, USA
*Corresponding author: john.c.brasunas@nasa.gov

Received 2 March 2015; revised 15 May 2015; accepted 18 May 2015; posted 18 May 2015 (Doc. ID 234654); published 8 June 2015

For accurate calibration of Fourier transform spectrometers we must constrain or resample the interferogram data to an invariant sampling comb. This can become challenging when instrument self-emission is significant and beam splitter absorption is present. The originally-sampled interferogram center-burst position can move due not only to sampling comb changes, but also to an interaction between the strength of an external target and the so-called anomalous phase (the two ports of the interferometer contribute center-bursts at different locations, and the relative weighting of the two ports varies with the strength of the external target). We present a model of the anomalous phase to enable partitioning of changes in observed center-burst location between sampling comb changes and anomalous phase effects.

OCIS codes: (120.3180) Interferometry; (120.6085) Space instrumentation; (120.6200) Spectrometers and spectroscopic instrumentation; (300.6300) Spectroscopy, Fourier transforms.

http://dx.doi.org/10.1364/AO.54.005461

1. INTRODUCTION

A linear Fourier transform spectrometer (FTS) such as Cassini CIRS [1–3] is calibrated via two calibration targets (typically deep space [cold] and an optics-temperature shutter [warm]) to infer response and self-emission terms. Each spectral resolution element is statistically independent and can be calibrated separately. Calibration is straightforward if conditions (response, self-emission, sampling comb) are stationary during the acquisition of shutter, deep space, and science targets. Calibration becomes more complex with the inclusion of random detector noise; resonant interfering features; sampling comb changes due to nonconstant moving mirror speed, spacecraft vibrations, laser mode-hops, and laser aging; thermally driven changes in CIRS; and aging of the CIRS instrument. A very basic requirement is that calibration be performed on effectively identically sampled interferograms.

About half of CIRS scans are science target scans, 40%–45% are deep space scans, and 5%–10% are shutter-closed scans. The shutter typically is closed every 4 h, however, acquisition of deep-space scans involves negotiations with the other Cassini science instruments for pointing control. Deep-space scans are typically available within 4 h from science scans, but occasionally the time offset may be as large as 24 h due to issues with the data quality (such as vibrations from the reaction wheel rates). For a given science observation, the number of nearby-time calibration scans (deep-space/shutter) will depend on the spectral resolution:

0.5 cm^{-1} 60–100/4–10 scans
3.0 cm^{-1} 100–300/15–50 scans
15. cm^{-1} 100–500/50–100 scans.

Thus the desire to go beyond stationary conditions for data calibration is sometimes strong, in order to average larger numbers of calibration target scans. To go beyond stationary conditions, we need to understand the sampling comb variations.

Typically one corrects for sampling comb shifts by calibrating in spectrum space and using classical phase correction techniques. When beam splitter (B/S) absorption is present, so-called vector calibration is required [4]. Classical phase correction would introduce errors because it does not partition observed shifts of the zero-path-difference (ZPD) location into shifts due to sampling comb changes versus shifts due to the anomalous phase that comes from B/S absorption coupled with changing input targets. We present below a partitioning procedure to enable a so-called "partial" phase correction/removal, identifying the changes in phase that are not due to sampling comb changes.

2. CIRS INSTRUMENT

CIRS (Fig. 1 and Table 1) records interferometric data in one direction of travel of its moving mirror at nearly constant speed. Incoming radiation at wavenumber σ is thus mapped to the electrical frequency f [5]

$$f = 2v\sigma, \tag{1}$$

for a single-passed moving mirror with speed v. For constant speed there is a fixed relation between electrical frequency and infrared wavenumber. CIRS has two distinct FTSs sharing a common moving mirror mechanism, with separate moving mirrors on either end of this mechanism. Figure 1 is a simplified drawing–not to scale. The FIR (far infrared) FTS includes FP1(detector focal plane 1) and is a polarizing design, with a linear grid of wires on a Mylar membrane for the B/S. Incoming unpolarized radiation is polarized by a grid, passed to a grid B/S which produces a variation of ellipticity as the mirror moves, and this changing ellipticity is converted to amplitude variation by the analyzer grid. The two FIR detectors are combined in antiseries to add their fringes, producing a single data stream for the FIR electronics. The MIR (mid infrared) FTS includes FP3 and FP4 with distinctly lower temperature detectors, and a conventional, compensated amplitude-division B/S (KBr). CIRS is designed to have a linear relationship between incoming infrared radiation and detector signal, S; CIRS infrared detectors were developed and tested to various performance requirements, including linearity. CIRS is temperature-controlled with internal heaters to assure quasi-stationary operating conditions to ease intensity calibration. In addition to signal, detector recorded voltages also include random noise N and interference resonances I. The noise is mostly detector Johnson (resistance) noise; interference may be the effect of voltages due to spacecraft or instrument currents, seen via shared grounding circuits [6]. The scan length (mostly to one side of ZPD) can be changed; the available range of (apodized) spectral resolution is approximately 15 to 0.5 cm^{-1}.

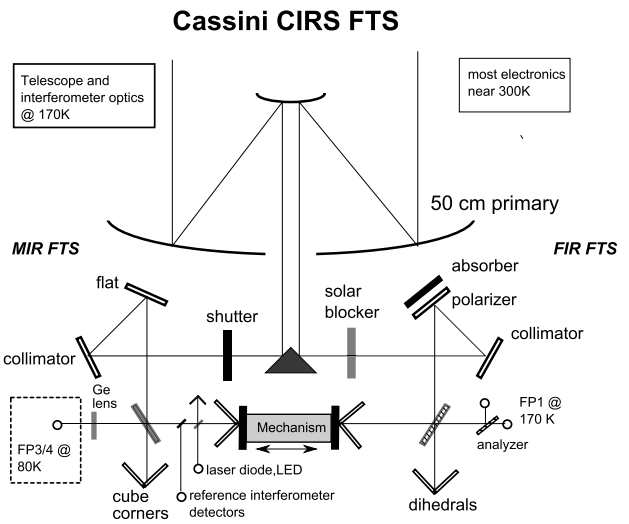

Fig. 1. CIRS has an MIR FTS and a FIR FTS sharing a common mechanism, and one calibration target (shutter–shown closed). Note the reference FTS within the MIR FTS.

CIRS has been acquiring data of the Saturnian system since orbital insertion in July of 2004, and this phase of the Cassini mission currently encompasses over 100 million interferograms. End of mission is anticipated in 2017. At any given time, data can be sent down from one, two or all three focal planes. In Table 1 the detector ID (identification) corresponds to various choices of five simultaneous detector channels (center detectors, odd/even, pairs).

ZPD, where the optical path differences between the fixed and moving arms is zero, is also called the white-light-point, because this is typically the one value of optical path difference where all the different wavelengths of a thermal (nearly incoherent) source add coherently in the interferogram to produce a global extremum (Fig. 2). Due to their band-limited nature (Table 1), FP3 and FP4 interferograms (Figs. 3 and 4, showing only the ZPD region) resemble sine-wave bursts after interpolation, sometimes with no clear global extremum–particularly for FP4.

Neither the FP3 nor the FP4 interferogram has a well-defined polarity. The CIRS interferograms would normally be sampled versus physical travel of the moving mirror according to the Nyquist criterion—at least twice per 2π-increment in optical path difference for the highest wavenumber. Due to their band-limited nature, FP's 3 and 4 are sampled less often (Table 1); half as often for FP3, and one third as often for FP4—aliasing does occur but without mixing spectral features, merely shifting the spectrum as a solid body in spectrum space to a lower wavenumber.

Table 1. The Isothermal FIR FTS (FP1) Needs One Calibration Target (Deep Space)[a]

CIRS focal plane	FP1 (FP2 descoped)	FP3	FP4
Bandpass (cm^{-1})	10–708.1 cm^{-1}	566.4–1132.9 cm^{-1}	1019.6–1529.4 cm^{-1}
Bandpass (Hz)	0.4–29.6 Hz	23.7–47.4 Hz	42.6–64.0 Hz
Nyquist interval	First	Second	Third
Detector	2 thermopiles—1 FOV	1 × 10 PC HgCdTe	1 × 10 PV HgCdTe
Detector ID	0	1–20	21–40
Pairs	NA	1–5	36–40
Central	NA	6–10	31–35
Odd/even	NA	11–20	21–30
Temperatures	Detector at 170 K optics at 170 K	detector at 80 K optics at 170 K	detector at 80 K optics at 170 K
Interfering spikes	Yes	Yes	No

[a]The MIR FTS (FP3, FP4) also needs the shutter target (Fig. 1).

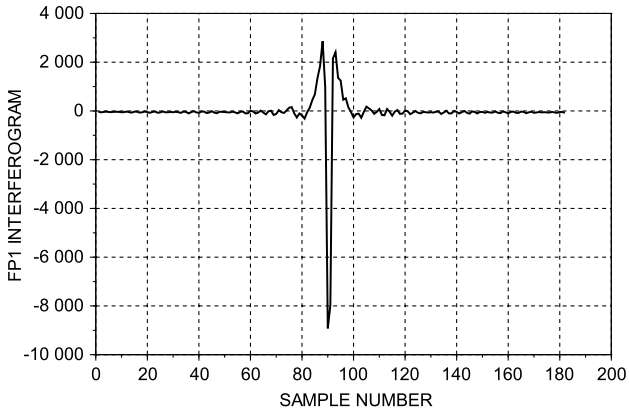

Fig. 2. Two-sided part of FP1 interferogram.

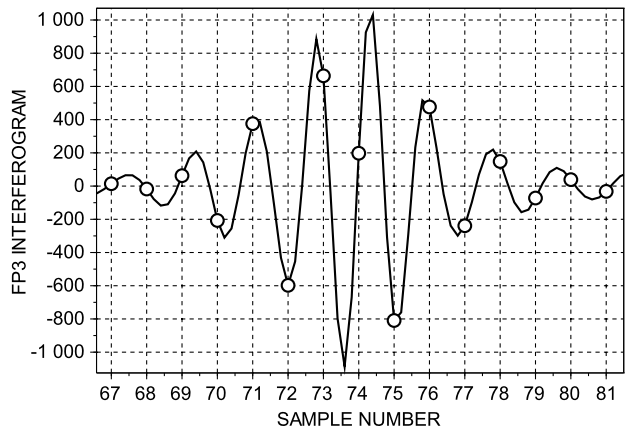

Fig. 3. FP3 interferogram (circles) and interpolated 5× (line).

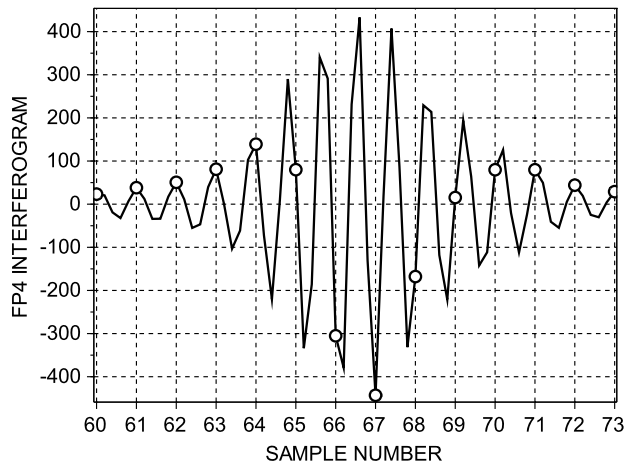

Fig. 4. FP4 interferogram (circles) and interpolated 5× (line).

3. OBSERVED BEHAVIOR OF CIRS ZPD

CIRS data are digitized at a high rate, and restricted to the desired band pass of Table 1 via numerical/digital filtering followed by resampling at a lower rate. The triggers for the CIRS sampling comb come from the reference interferometer [7] within the MIR FTS (Fig. 1). Zero-crossings of the laser signal (~785 nm near 170 K) drive the raw sampling of the infrared detectors, and the start of sampling is triggered by a light-emitting diode (white light signal). A fractional value for ZPD location, denoted "nzpd," is calculated from the resampled data by fitting a parabola to interpolated versions (200-fold) of the resampled interferograms. Over the course of the mission when CIRS is turned off and then on, the laser may not start in the same mode, changing somewhat the laser wavelength. Typically, CIRS may be in the same mode for a year or so [8]. This paper will be mostly restricted to scans in 2011, where the science target and calibration scans are all taken in the same laser mode (same laser wavelength). Thus, all sampling-comb corrections are shifts.

After the sampling comb for the infrared signals is enabled by the light-emitting diode signal from the reference interferometer and clocked by zero-crossings of the diode laser fringes, there is scan-to-scan variability of nzpd due to the effects listed in Table 2 (from largest to smallest for FP4). The last row of Table 2 lists the magnitude of nzpd mismatch during calibration that results in a continuum error equal to 1% of the strongest features in a Titan spectrum. The following discussions are brief to place in context the target-effect, which is described in greater detail.

A. Finding the Wrong Peak (FP3, FP4)

No matter what rule we pick (largest positive peak, largest negative peak, largest absolute value of the peaks in Figs. 3 or 4), when we construct a time history of ZPD we find that while most ZPD values lie within a relatively narrow range, some are clearly offset by the peak-to-peak spacing in the sine-wave bursts. As all other ZPD changes are much smaller than this, these peak-to-peak excursions self-identify themselves as errors of the algorithm. Therefore, in our first pass over time we choose some rule, then on our second pass we identify the outliers and choose a nearby peak to minimize the observed jumps. This difficulty is a function of FP3 and FP4 being narrow bands.

B. Target Effects: Anomalous Phase and Chirping

These are real effects in the measured ZPD, but not sampling comb changes. The magnitude of this effect is bounded by the shutter effect (Fig. 5), as almost all our science targets are small compared with the 170 K blackbody shutter. The challenge is to predict this effect when looking at a science target of unknown amplitude. A model for the target effect will be presented below. In Fig. 5, the baseline corresponds to deep space scans, the largest positive excursions are shutter-closed scans, and intermediate positive excursions are due to science targets.

To distinguish anomalous phase from chirping, and thus to know whether we must employ vector calibration, we need to look at the spectra. Considering just the two-sided parts of FP4 (detector ID 25 of Table 1) calibration scans, we plot the un-calibrated amplitudes in Fig. 6(a) and the phase difference in Fig. 6(b). The nonzero phase difference indicates this is an anomalous phase issue, and vector calibration must be used. Had it been chirping, the phase would not change (or it would

Table 2. Typical Values for nzpd and nzpd Variations

nzpd	**FP1**	**FP3**	**FP4**	
Typical nzpd	89.2	72.6	65.5	ZPD location after processing
Scale of nzpd change	**FP1**	**FP3**	**FP4**	**Comments**
Finding wrong peak (signed)	NA	1.6	0.9	Algorithm failure (Figs. 3, 4)
Shutter open/shutter closed (maximum target effect)	NA	0.08	0.2	Anomalous phase **Not a sampling comb change**
Isolated glitches (typically single scan)	0.11	0.09	0.08	Shift within stable sample comb Usual shift is two raw samples Data may have other problems
Laser mode change (step change)	0.019	0.016	0.014	Sample comb **stretch** A step change every ~year or so
Long-term year-to-year drift	Oscillatory	~0.015	0.01	Over 5 years—seems to be a shift
Temperature variations Time scale of hours	0.04	0.007	0.006	Sample comb shift Detectors correlated within FP Depends on thermal gradients, speed variations; vibrations
Short-term stability Scan-to-scan		0.005	0.005	Low correlation among detectors
1% spectrum error	0.1	0.001	0.001	Tolerance for comb mismatch

change by π for a polarity change); the observed phase change is near $\pi/2$. The phase difference for FP3 (Fig. 7) is closer to π, but distinctly offset. The phase difference for FP1 (deep space versus a strong natural target, Fig. 8) is close to zero (modulo 2π). Chirping is minimized in CIRS FP3 and 4 due to the narrow band-pass nature and the similar spectral content of self-emission and the shutter target (both at 170 K).

C. Isolated ZPD Glitches

The downward spikes in Fig. 5 are shifts of the sampling comb. This is verified by looking at shifted and unshifted shutter scans, noting that their Fourier transforms have identical (to within the noise) amplitudes and a phase difference linearly proportional to wavenumber. Most of these shifts typically have the same amplitude, corresponding to two-raw-sample shifts as noted in Table 2. These shifted scans are more prevalent for particular rotation rates of one of the Cassini spacecraft reaction wheels.

D. Laser Mode Changes

Under normal operating conditions, the CIRS optics are stabilized to ~0.1 K near 170 K; the time scale for a solar-driven large temperature change is ~24 hours. As described in [8], the CIRS reference laser remains in a single mode except during an instrument turn-off/turn-on every year or so, some scheduled and some not. At turn-off/turn-on, the laser may come up in a different mode, changing the sampling comb spacing and creating a step-change in nzpd. This is a stretch or destretch of the sampling comb, not a shift.

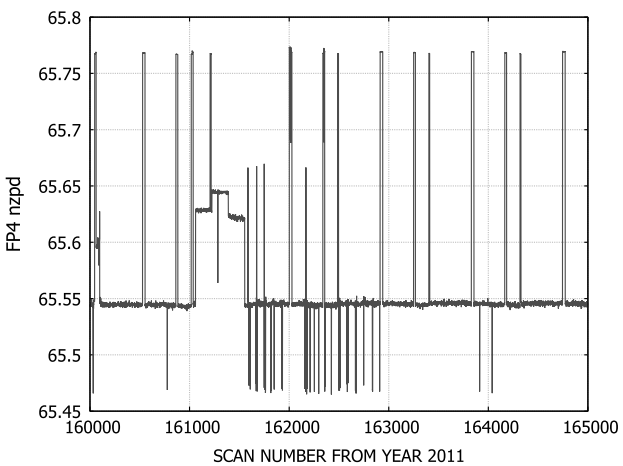

Fig. 5. Large positive nzpd excursions are due to switching from deep space target to shutter closed (detector 25). The negative excursions are sampling comb shifts.

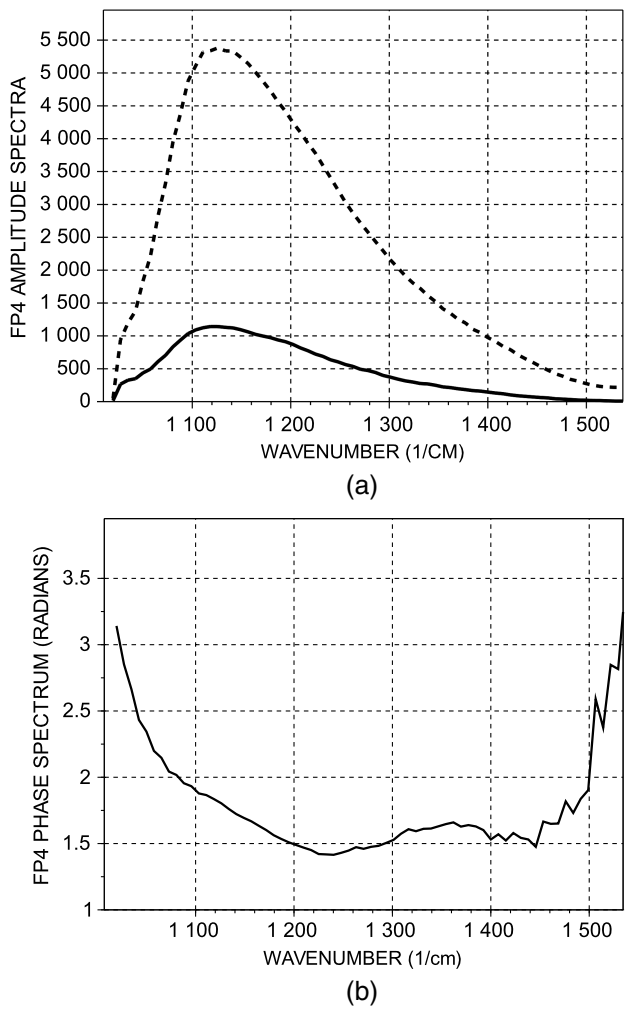

Fig. 6. (a) Deep space (solid) and shutter (dotted). (b) Phase difference: deep space/shutter.

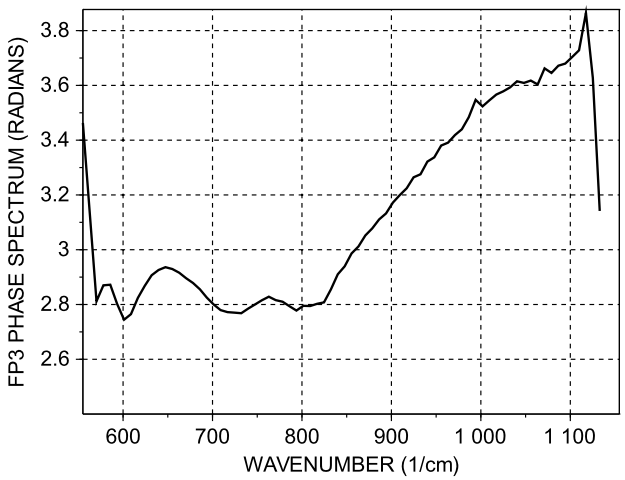

Fig. 7. Phase difference: deep space/shutter.

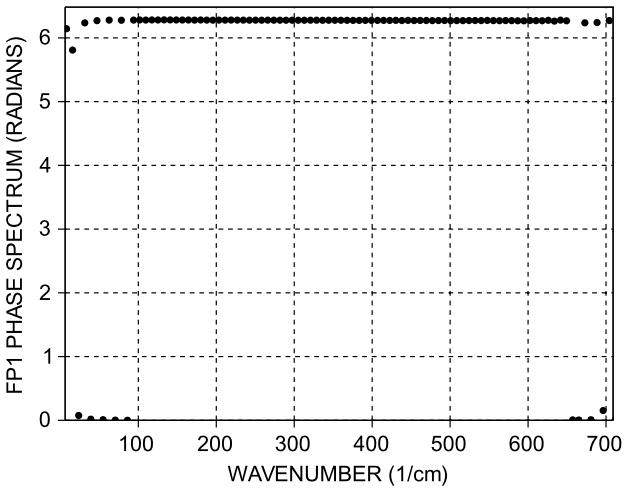

Fig. 8. Phase difference: deep space/strong external target.

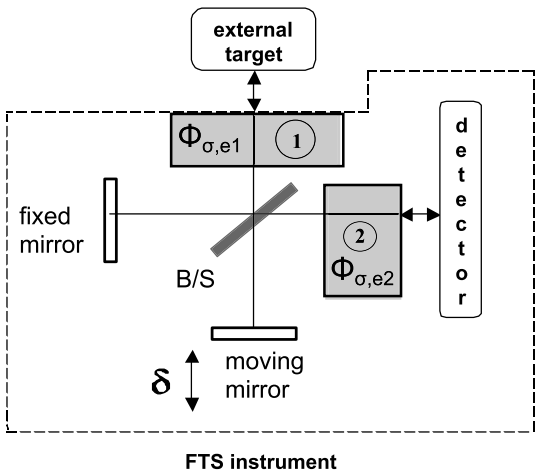

Fig. 9. Model for FTS internal emission from entrance port (1) and detector port (2).

E. Long-Term Drift

FP1, FP3, and FP4 show long-term (year-to-year) drifts in nzpd, which can be viewed as a form of aging. From an analysis based on monitoring the Mylar B/S features in FP1 [8] we can determine that there is no long-term drift of the spectral location of the Mylar features, so this is a shift and not a stretch.

F. Temperature Variations (Hourly Scale)

nzpd appears to have little or no dependence on CIRS temperatures, but there does appear to be a weak dependence for FP3 and FP4 on temperature gradients–driven internally by the moving mirror mechanism or externally by solar and planetary illumination. FP1 does have substantial thermally-driven nzpd excursions, but FP1 can be calibrated via scalar equations.

G. Short-Term Stability

On a less than 1-hour time-scale, the single-scan estimate of nzpd appears to show random variation, scan to scan. The simultaneously-recorded five channels of each focal plane also show low correlation, channel-to-channel.

4. MODEL FOR THE FTS INTERFEROGRAM IN THE PRESENCE OF B/S ABSORPTION

Various groups have presented a variety of ways to handle complex calibration in the case of a nonconstant sampling comb. These techniques include constraints on the real and imaginary parts of interferogram spectra [9], analytical models [10], and techniques for extracting ZPD shifts [11,12]. These approaches are largely based on analysis of spectra. Here we take a different approach. Due to the large number of interferograms so far (over 100 million), we seek to separate sampling-comb shifts from anomalous phase effects by studying the behavior of the measured ZPD location (nzpd), thus we are mostly looking at the interferograms.

An FTS is a two-input-port, two-output-port system (Fig. 9). When a nonisothermal FTS (such as CIRS. FP3. and FP4). has absorption between the events where the incoming infrared radiation is split and then recombined, such as in the B/S, it is no longer the case that emission from ports 1 and 2 reach the detector focal plane 180 degrees apart. The extra phase (the deviation from 180) is roughly equivalent to saying that the interferogram signals from the two input ports do not have the same ZPD location [13]. A change in the strength of the external target will make ZPD appear to shift, all other things being equal. In this case, the fringe-modulated spectral radiant flux (or spectral radiant power) reaching the detector in port 2 satisfies Eq. (14) in Ref. [13] (assuming no instrument self-emission except for the B/S and a unity-emissivity detector; also assuming a unity-emissivity external target):

$$dF_{\mathrm{mod}} = 2RT\{F_{\mathrm{tar}}\cos\delta - F_{B/S}[\cos\delta + \cos(\delta - \Delta)] + F_{\mathrm{det}}\cos(\delta - \Delta)\}. \quad (2)$$

R and T are the power reflection and transmission of the B/S, δ is the round-trip optical path-difference expressed as a phase in radians, and $\Delta = 2(\delta_t - \delta_r)$, twice the difference of the phases of the complex transmission and reflection amplitudes of the B/S (π for a loss-less dielectric). δ is defined as

$$\delta = 2\pi(2\sigma d), \quad (3)$$

where σ is the wavenumber of interest, and d is the physical distance the moving mirror has moved from ZPD. F_{tar}, $F_{B/S}$, and F_{det} are the unity emissivity spectral radiant powers (conventionally denoted Φ_σ) of the external target, B/S and detector, for example

$$F_{B/S} == \Phi_{\sigma,B/S} = A\Omega B(\sigma, T_{B/S}), \tag{4}$$

where $A\Omega$ is the FTS etendue and B is the Planck function at wavenumber σ and temperature $T_{B/S}$. Using Φ_σ rather than F, using $\Phi_\sigma^{\text{fringe}}$ for the fringe-modulated spectral flux dF_{mod}, and including a term M for the FTS fringe efficiency relating to flatness of the B/S and end mirrors of the FTS arms and their relative alignment, we re-express Eq. (2) as

$$\Phi_\sigma^{\text{fringe}} = 2\text{MRT}\{[\Phi_{\sigma,\text{tar}} - \Phi_{\sigma,B/S}]\cos\delta - [\Phi_{\sigma,\text{det}} - \Phi_{\sigma,B/S}]\cos(\delta - \Delta_\pi)\}, \tag{5}$$

where $\Delta_\pi = (\Delta - \pi)$, a measure of the phase anomaly due to B/S absorption. Including low-emissivity terms $\varepsilon_1\Phi_{\sigma,e1}$ and $\varepsilon_2\Phi_{\sigma,e2}$ for emissive mirror surfaces or filters in the two FTS ports, and letting the external target have the emissivity ε_{tar}, we then have

$$\begin{aligned}\Phi_\sigma^{\text{fringe}} = 2\,\text{MRT}(1-\varepsilon_2)\{&[(1-\varepsilon_1)\varepsilon_{\text{tar}}\Phi_{\sigma,\text{tar}} \\ &+ \varepsilon_1\Phi_{\sigma,e1} - \Phi_{\sigma,B/S}]\cos\delta - [(1-\varepsilon_2)\Phi_{\sigma,\text{det}} \\ &+ \varepsilon_2\Phi_{\sigma,e2} - \Phi_{\sigma,B/S}]\cos(\delta - \Delta_\pi)\}.\end{aligned} \tag{6}$$

5. APPLYING THE MODEL TO CIRS FP3, FP4

For each spectral interval at σ, the modulated part of the FTS interferogram is

$$I_{\sigma,\text{mod}} = \mathcal{R}\Phi_\sigma^{\text{fringe}}, \tag{7}$$

where $\mathcal{R}$ is the detector responsivity in volts/watt. Following Eq. (6), from the two ports there are two ZPD locations, offset by Δ_π. As we know from Table 1, both FP3 and FP4 are band-limited channels, so we can start by approximating FP3 and FP4 as single spectral-resolution elements. Combining Eqs. (4), (6), and (7), assuming the FTS port 1 and port 2 emissive surfaces are at the B/S temperature, dropping the $\Phi_{\sigma,\text{det}}$ term due to its low temperature and the high wavenumbers of FP3 and FP4, and defining $k = 2\text{MRT}(1-\varepsilon_2)\,\mathcal{R}\Phi_{\sigma,B/S}$ we have

$$I_{\sigma,\text{mod}} = k\left\{\left[(1-\varepsilon_1)\varepsilon_{\text{tar}}\frac{B(\sigma, T_{\text{tar}})}{B(\sigma, T_{B/S})} + \varepsilon_1 - 1\right] \times \cos\delta - [\varepsilon_2 - 1]\cos(\delta - \Delta_\pi)\right\}. \tag{8}$$

Using Eq. (3) and defining

$$t = (1-\varepsilon_1)\varepsilon_{\text{tar}}\frac{B(\sigma, T_{\text{tar}})}{B(\sigma, T_{B/S})}, \tag{9}$$

then

$$I_{\sigma,\text{mod}} = k\{[1-\varepsilon_2]\cos[(4\pi\sigma d) - \Delta_\pi] - [1-\varepsilon_1 - t]\cos[4\pi\sigma d]\}. \tag{10}$$

The usual strongest target $\Phi_{\sigma,\text{tar}}$ corresponds to the emission from the CIRS shutter at 170 K, so the usual range of t is from zero (deep space) to near-unity. As the intensity of the external target changes, we change the degree to which the net interferogram is steered to the ZPD of either port 1 or port 2.

Equation (10) represents the measured interferogram as a function of moving-mirror position d. The interferogram is the difference of two cosines with the same spatial frequency, but different amplitudes and phases. The net amplitude and phase has a complicated dependence on the external target $\Phi_{\sigma,\text{tar}}$ through Eq. (9) and the terms in Eq. (10). It is easier to calculate amplitude and phase if we first convert Eq. (10) to a corresponding complex form whose real part is the original, real expression. Had Eq. (10) been equal to $A\cos(4\pi\pi\text{d} + \varphi)$, the corresponding complex form would have been $A\exp[i(4\pi\pi\text{d} + \varphi)]$. Note that the real form and the complex form have the same amplitude and phase. The advantage of going to complex form is that it is easier to manipulate complex expressions to derive the net amplitude and phase. The complex form of the interferogram is:

$$I_{\sigma,\text{complex}} = k\{[1-\varepsilon_2]\exp[i(4\pi\sigma d - \Delta_\pi)] - [1-\varepsilon_1 - t]\exp[i4\pi\sigma d]\}, \tag{11}$$

or

$$I_{\sigma,\text{complex}} = \exp[i4\pi\sigma d]\text{cburst}(t), \tag{12}$$

where

$$\text{cburst}(t) = k\{[1-\varepsilon_2]\exp[-i\Delta_\pi] - [1-\varepsilon_1 - t]\}. \tag{13}$$

The phase shift of the interferogram relative to the sampling comb with no phase anomaly ($\Delta_\pi = 0$), and the amplitude of the interferogram at ZPD position, are given by the phase and amplitude of cburst(t). For shutter-closed ($t = 1 - \varepsilon_1$), the phase shift is $-\Delta_\pi$. For deep-space ($t = 0$), if $\varepsilon_1 \sim \varepsilon_2$, after some trigonometric manipulations we see that the phase shift is $-\pi/2 - \Delta_\pi/2$. Therefore the phase difference between deep-space and shutter-closed scans is $-\pi/2 + \Delta_\pi/2$, which is consistent with what we saw in Section 3 for FP4 if the FP4 anomalous phase is small.

By taking derivatives it may be confirmed that the minimum *cburst* amplitude, *ampmin*, occurs at t_{min} when the real part of *cburst* is zero:

$$[1-\varepsilon_2]\cos[\Delta_\pi] = [1-\varepsilon_1 - t_{\text{min}}], \tag{14}$$

$$t_{\text{min}} = (1-\varepsilon_1) - (1-\varepsilon_2)\cos(\Delta_\pi). \tag{15}$$

For *ampmin* to be observable, t_{min} must be non-negative; this is true if

$$\varepsilon_1 < \varepsilon_2\cos\Delta_\pi + (1 - \cos(\Delta_\pi)). \tag{16}$$

Since *ampmin* corresponds to *cburst* being purely imaginary, then

$$\text{ampmin} = k(1-\varepsilon_2)|\sin\Delta_\pi|. \tag{17}$$

We may re-express *cburst* as

$$\text{cburst}(t) = \frac{\text{ampmin}}{|\sin\Delta_\pi|}\left\{\exp[-i\Delta_\pi] - \frac{1-\varepsilon_1 - t}{1-\varepsilon_2}\right\}. \tag{18}$$

Eq. (18) gives us the amplitude and phase offset of the interferogram peak at ZPD, as a function of the external signal t. To convert the phase offset to a change in the nzpd (dnzpd/dphase), we must refer to Figs. 3 and 4. Given our approximation of FP3 and FP4 being sinewave-like, the change in nzpd

between adjacent peaks of the same polarity corresponds to a phase change of 2π, providing an estimate of dnzpd/dphase. The model nzpd(t) as a function of t is therefore

$$\mathrm{nzpd}(t) = \frac{\mathrm{dnzpd}}{\mathrm{dphase}}\{\arg[\mathrm{cburst}(t)] - \frac{\pi}{2}\,\mathrm{sgn}(\Delta_\pi)\} + \mathrm{natmin} \tag{19}$$

where the *arg* function retrieves the phase in radians of a complex quantity, *sgn* is the sign function, $(\pi/2)\ \mathrm{sgn}(\Delta_\pi)$ is the phase of *cburst* at minimum amplitude when it is purely imaginary, and *natmin* is the value of nzpd corresponding to amplitude *ampmin*.

Observing a nonzero *ampmin* is an indicator of anomalous phase (in a nonisothermal detector/optics system). A comparison of FP4 (amplitude, nzpd) year 2011 data pairs of the observed center-bursts and the target-effect model is given in Fig. 10 for $\Delta_\pi = 0.21$ radians; curvature in this relationship is another indication of anomalous phase. Getting a good fit between data and the model constrains all the model parameters except ε_1 and ε_2; the relative values of these two emissivities are constrained via Eq. (15), to produce an estimate of $t_{\min}$ consistent with the data. The weakest external target (deep space) occurs near (475, 65.55), and the data describe a clockwise arc for stronger targets. Minimum amplitude is observed for $t_{\min}$ near zero, meaning ε_1 and ε_2 are nearly balanced via Eq. (15). The strongest natural targets (amplitude ~1000) are typically Titan scans, and the shutter scans are near amplitude ~2200. A secondary data arc is displaced downward due to the two-raw-sample shift effect. Other data weaker than amplitude ~475 correspond to reaction wheel disturbances and/or elevated focal plane temperatures (which have been mostly excluded from Fig. 10).

The corresponding situation for FP3 is shown in Fig. 11; the anomalous phase is weaker (−0.06 radians). Here deep space corresponds to amplitude ~1080. For stronger targets the center-burst starts to weaken, but the model-fit-turnaround shows that minimum amplitude is not observed due to stronger self-emission ε_2 in the detector port (emissivities $\varepsilon_1 = 0.06$ and $\varepsilon_2 = 0.28$ were used, but the fit mostly constrains their

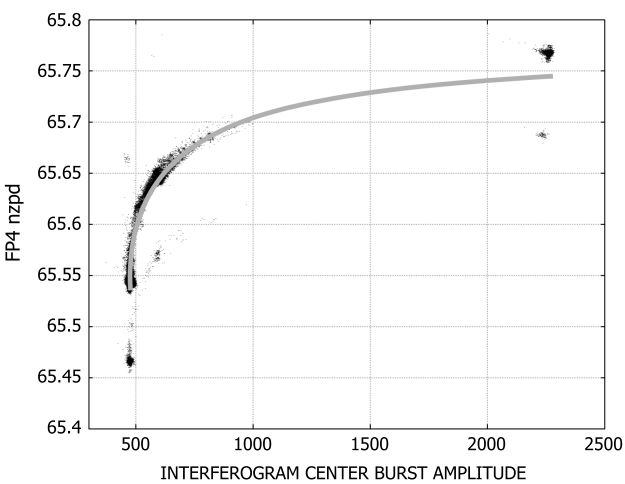

Fig. 10. (FP4[25] nzpd [black] compared with the theoretical model of Eq. (8) [gray line].

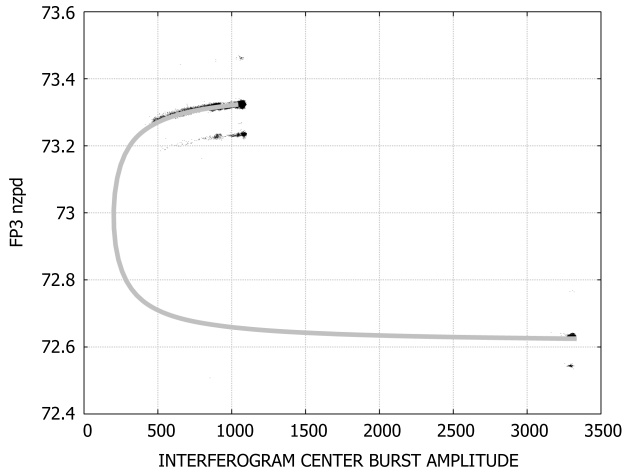

Fig. 11. FP3[14] nzpd [black] compared with the theoretical model of Eq. (8) [gray line].

difference). The emissivity imbalance is likely due to the Ge lens and filter coatings (Fig. 1). In addition to the two-raw-sample effect giving a lower curve, there are also some higher spots at the deep space amplitude (~1080) due to sampling shifts with a sign opposite to the usual two-raw-sample offset, also due to reaction wheel effects.

The FP4 model misses the shutter-closed scans by ~0.02 in nzpd. Since the match to shutter-closed is much closer for FP3 (Fig. 11), we interpret this as a weakness in the anomalous-phase model rather than a real change in the sampling comb.

6. REVIEW AND SUMMARY

If the sampling comb is not changing, then calibration is straightforward because interferograms can be subtracted, and calibration becomes a one-port problem, amenable to scalar calibration (classical phase correction). If the sampling comb is changing, scalar calibration is also valid if there is no B/S absorption. However, when B/S absorption is present, the sampling comb is varying, and the instrument is not isothermal (detector and optics), then the changes observed in the sampled center-burst location must be partitioned into sampling comb changes and anomalous phase effects.

We have demonstrated this partitioning for the Cassini CIRS FTS, modeling the anomalous phase effect in the context of the many, real changes in the CIRS sampling comb. A simple model of the anomalous phase based on the individual emissivities of the two FTS ports accounts well for the dependence of the center-burst position on the center-burst amplitude. Plotting center-burst position versus amplitude allows us to distinguish sampling comb changes from anomalous phase effects. On the simplest level, this enables identification of interferograms that are questionable due to environmental influences such as micro-vibrations and temperature changes.

For interferograms deemed usable, the anomalous phase model enables us to assign an anomalous phase to each interferogram as a function of center-burst amplitude. On a scan-by-scan basis, the difference between the anomalous phase and the total phase is an estimate of the time-varying changes of the

sampling comb. Undoing these changes makes possible the production of large averages of interferograms, in particular of calibration targets, with a corresponding decrease in statistical uncertainties.

APPENDIX A: ACRONYMS

B/S: beam splitter
FIR: far infrared
FP: focal plane
FTS: Fourier transform spectrometer
MIR: mid infrared
nzpd: interferogram sample number at ZPD (interpolated)
ZPD: zero path difference between two arms of FTS

REFERENCES

1. V. Kunde, P. Ade, R. Barney, D. Bergman, J. F. Bonnal, R. Borelli, D. Boyd, J. Brasunas, G. Brown, S. Calcutt, R. Courtin, J. Cretolle, J. Crooke, M. Davis, S. Edberg, R. Fettig, M. Flasar, D. Glenar, S. Graham, J. Hagopian, C. Hakun, P. Hayes, L. Herath, L. Horn, D. Jennings, G. Karpati, C. Kellebenz, B. Lakew, J. Lindsey, J. Lohr, J. Lyons, R. Martineau, A. Martino, M. Matsumura, J. McCloskey, T. Melak, G. Michel, A. Morell, C. Mosier, L. Pack, M. Plants, D. Robinson, L. Rodriguez, P. Romani, W. Schaefer, S. Schmidt, C. Trujillo, T. Vellacott, K. Wagner, and D. Yun, "Cassini infrared Fourier spectroscopic investigation," Proc. SPIE **2803**, 162–177 (1996).
2. F. M. Flasar, V. G. Kunde, M. M. Abbas, R. K. Achterberg, P. Ade, A. Barucci, B. Bezard, G. L. Bjoraker, J. C. Brasunas, S. Calcutt, R. Carlson, C. J. Cesarsky, B. J. Conrath, A. Coradini, R. Courtin, A. Coustenis, S. Edberg, S. Edgington, C. Ferrari, T. Fouchet, D. Gautier, P. J. Gierasch, K. Grossman, P. Irwin, D. E. Jennings, E. Lellouch, A. A. Mamoutkine, A. Marten, J. P. Meyer, C. A. Nixon, G. S. Orton, T. C. Owen, J. C. Pearl, R. Prange, F. Raulin, P. L. Read, P. N. Romani, R. E. Samuelson, M. E. Segura, M. R. Showalter, A. A. Simon-Miller, M. D. Smith, J. R. Spencer, L. J. Spilker, and F. W. Taylor, "Exploring the Saturn system in the thermal infrared: the composite infrared spectrometer," Space Sci. Rev. **115**, 169–297 (2004).
3. J. C. Brasunas and B. Lakew, "Long-term stability of the Cassini Fourier transform spectrometer en route to Saturn," in *Recent Research Developments in Optics*, A. Gayathri, ed. (Research Signpost, 2004), Vol. **4**, pp. 95–113.
4. H. E. Revercomb, H. Buijs, H. B. Howell, D. D. Laporte, W. L. Smith, and L. A. Sromovsky, "Radiometric calibration of IR Fourier transform spectrometers: solution to a problem with the high-resolution interferometer sounder," Appl. Opt. **27**, 3210–3218 (1988).
5. J. C. Brasunas, V. G. Kunde, and L. W. Hearth, "Cryogenic Fourier spectrometer for measuring trace species in the lower stratosphere," Appl. Opt. **27**, 4964–4976 (1988).
6. C. Chan, S. Albright, N. Gorius, J. Brasunas, D. Jennings, F. M. Flasar, R. Carlson, E. Guandique, and C. Nixon, "Electrical Interferences observed in the Cassini CIRS spectrometer," Exp. Astron., doi: 10.1007/s10686-015-9452-3 (to be published).
7. A. J. Martino and D. M. Cornwell, "Reference interferometer using a semiconductor laser/LED reference source in a cryogenic Fourier-transform spectrometer," Proc. SPIE **3435**, 61–71 (1998).
8. J. C. Brasunas, "Laser mode behavior of the Cassini CIRS Fourier transform spectrometer at Saturn," Infrared Phys. Technol. **55**, 533–537 (2012).
9. A. Kleinert and O. Trieschmann, "Phase determination for a Fourier transform infrared spectrometer in emission mode," Appl. Opt. **46**, 2307–2319 (2007).
10. G. Bianchini, L. Palchetti, and B. Carli, "Vectorial combination of signals in Fourier transform spectroscopy," Infrared Phys. Technol. **52**, 19–21 (2009).
11. S. Turbide and T. Smithson, "Calibration algorithm for Fourier transform spectrometer with thermal instabilities," Appl. Opt. **49**, 3411–3417 (2010).
12. B. Saggin, D. Scaccabarozzi, and M. Tarabini, "Instrumental phase-based method for Fourier transform spectrometer measurements processing," Appl. Opt. **50**, 1717–1725 (2011).
13. J. C. Brasunas, "Phase anomalies in Fourier-transform spectrometers: an absorbing beam splitter is neither sufficient nor necessary," Appl. Opt. **41**, 2481–2487 (2002).